ELSEVIER

Contents lists available at ScienceDirect

Physics of the Earth and Planetary Interiors

journal homepage: www.elsevier.com/locate/pepi





Reversal of drift direction during the Laschamp geomagnetic excursion

Nicole Clizzie*, Catherine Constable

Cecil H. and Ida M. Green Institute of Geophysics & Planetary Physics, Scripps Institution of Oceanography, University of California San Diego, 9500 Gilman Drive, La Jolla 92093, CA, United States

ARTICLE INFO

Keywords:
Paleomagnetic secular variation
Westward drift
Eastward drift
Geodynamo
Reverse magnetic flux patches
Paleomagnetic field model

ABSTRACT

Earth's magnetic field changes in both space and time: the temporal changes are called geomagnetic and paleomagnetic secular variations. Westward drift has been noted as a feature of secular variation for several centuries, but eastward drift has received less attention. We use three global geomagnetic field models covering the past $100 \, \text{kyr}$ to extend temporal coverage for tracking the zonal (azimuthal) motion of the radial magnetic field. The models we use are GGF100k ($100-0 \, \text{ka}$), GGFSS70 ($70-15 \, \text{ka}$), LSMOD.2 ($50-30 \, \text{ka}$); the extent of the models enables the inclusion of the extreme secular variations found during excursions, particularly the Laschamp excursion ($42-40 \, \text{ka}$). GGFSS70 and LSMOD.2 have higher temporal resolution than GGF100k, but their underlying data have poorer spatial coverage. Spatial structure is greatly diminished in all models for spherical harmonic degrees l > 4.

We use two types of time-longitude plots, one of the full radial field to expose reverse and intense flux patches at the core-mantle boundary. The second time-longitude plot is processed to enhance zonal motion signatures and allows us to use Radon drift analyses to uncover characteristic time scales of both westward and eastward drift at mid to high latitudes in both the northern and southern hemispheres. Our results differ across the three models, which we attribute to varying degrees of resolution, accuracy, and data distribution. Nevertheless, recurrent episodes of both eastward and westward drift ranging from $\pm 0.05^{\circ}/\text{yr}$ to $\pm 0.18^{\circ}/\text{yr}$ occur in both the northern and southern hemispheres. Westward drift dominates. We also observe 8–20 kyr intervals between occurrences of high-latitude reverse flux patches correlated with strong drift signals. Focusing on the period 50–30 ka, we observe dominant eastward drift preceding the Laschamp excursion and westward drift subsequently. In a period not associated with an excursion, 90–80 ka, we see strong mid to high latitude drift signatures in the northern hemisphere.

1. Introduction

The convecting fluid in the Earth's outer core generates the magnetic field and its secular variation. Observation of field changes is essential to understanding the geodynamo and how it can be self-sustaining. One well-known feature of secular variation is westward drift (Bullard et al., 1950), while eastward drift is less prominent. Proposed mechanisms for zonal (azimuthal) drift are fluid motion in the core transporting magnetic flux, propagation of magnetohydrodynamic waves, or a combination of both (Finlay and Jackson, 2003). In the modern field, Pais and Jault (2008) uncovered a high northern latitude jet near the tangent cylinder moving westward dominantly over Canada and Alaska. Another type of large-scale flow in the modern field is represented by gyres (e.g., Finlay et al. (2016); Barrois et al. (2018); Pais and Jault (2008)). These gyres are prominent in the Atlantic hemisphere: in the

southern hemisphere, flow moves anticyclonically with boundaries near Antarctica, the eastern Indian Ocean, and Chile; in the northern hemisphere, flow moves anticyclonically with boundaries over east Asia, northern Africa, and North America. Hide (1966) first proposed slow magnetic Rossby waves as the mechanism for westward drift. Hori et al. (2015) re-examined zonal motion in the context of recent numerical dynamo simulations and showed slow Rossby waves riding on the advective mean flow. Slow Rossby wave modes are linked to Alfven frequency and are sensitive to both toroidal (Hori et al., 2022; Hori et al., 2018; Hori et al., 2019) and poloidal field strength (Gerick et al., 2021; Gillet et al., 2022). The timescales of these waves range from decades to multiple millennia.

Assessing centennial to multi-millennial secular variation features is accomplished by reconstructing the paleomagnetic field through time-varying field models built from records in sediment cores, archeo-

E-mail address: nclizzie@ucsd.edu (N. Clizzie).

^{*} Corresponding author.

logical artifacts, and lava flows. Previous studies have used paleomagnetic field models to track zonal motion, but the extent of the field models used does not capture any extreme secular variation events such as excursions. Within the past 100 kyr, there have been several excursions, some sparsely documented and others agreed upon: Hilina Pali (\sim 17 ka), Mono Lake/ Auckland (\sim 33 ka), Laschamp (\sim 41 ka), Norwegian-Greenland Sea (\sim 61 ka), post-Blake (\sim 95 ka) (Laj and Channell, 2015, p. 345–356).

Observation of westward drift dates back to Edmond Halley, who noted the westward migration of magnetic features (Halley, 1692; Halley, 1683). Reviews of the subject of drift can be found in Constable and Korte (2015, p. 328) and Holme (2015, p. 92), but here we limit ourselves to a brief overview of studies using time-longitude plots derived from time-varying spherical harmonic models to uncover zonal drift. Finlay and Jackson (2003) were the first to use a time-longitude plot to track zonal magnetic flux at the core mantle-boundary (CMB) for the past four centuries using the gufm1 field model (Jackson et al., 2000). They found persistent westward drift of 0.27°/yr in the equatorial region. In another study tracking zonal motion, Dumberry and Finlay (2007) used the now superseded CALS7k.2 model (covering 7–0 ka) (Korte and Constable, 2005). They found both eastward and westward drift at mid to high latitudes in the northern hemisphere for the past 3000 years and a lack of model resolution in equatorial regions. They suggested transition of the direction of zonal motion is linked to archaeomagnetic jerks (Gallet et al., 2003, 2009). A more recent study of tracking zonal motion is by Nilsson et al. (2020) using the pfm9k.1a paleomagnetic field model for the past 9000 years (Nilsson et al., 2014). They found persistent high-latitude westward drift signals in both hemispheres. In the northern hemisphere, they isolated two distinct westward propagating waveforms of $-0.09^{\circ}/\text{yr}$ and $-0.25^{\circ}/\text{yr}$ with wavenumbers of order m = 2 and m = 1, respectively.

Our study extends the tracking of zonal motion to the past 100,000 years using three paleomagnetic field models (PFMs), GGF100k (Panovska et al., 2018), GGFSS70 (Panovska et al., 2021), and LSMOD.2 (Korte et al., 2019). First, we briefly describe the PFMs, highlighting the inversion methods used in their construction, data coverage, and attainable resolutions. Next, we illustrate the use of time-longitude plots, and Radon drift determination methods on a numerical dynamo simulation. We present time-longitude plots of the full radial field to show high-latitude reverse and weak fields that occur for the past 100 ka. We also show the changes in strength and rate of zonal drift in the form of moving averages over time. In the main text, we focus on the interval 50–30 ka and 90–80 ka by presenting the time-longitude plots of processed models and global variations of drift rate. We discuss the robustness and differences in the results across the PFMs, and the zonal motion during the Laschamp excursion and a quiet period (e.g., 90–80 ka).

2. Paleomagnetic field models

Our three time-varying global geomagnetic field models are reconstructed from sediment records, archaeomagnetic data, and lava flows and cover various segments of the past 100 ka. For each model, distinct "constructive choices" were made to handle the regional sediment rate differences, data quality (e.g., sediment rate; dating; accuracy of magnetic record), and quantity (e.g., global distribution; regional density; temporal distribution). Additional constructive choices (e.g., smoothing kernel in forward modeling; regularization; misfit level; knot spacing; stacking of regional sediment records; selection and calibration of sediment records) are intertwined with the primary data selection and contribute to both resolution and accuracy. The constructive choices for each model are described briefly below.

Each model is parameterized in space with spherical harmonics (SH) and in time with cubic B-splines (e.g., Jackson and Finlay (2015), Section 5.05.3)). The PFMs are regularized field models with a trade-off between data misfit and model spatial and temporal smoothness. The

regularization determines the spatial and temporal resolution by minimizing complex field structures as measured by the ohmic diffusion norm (Gubbins, 1975).

2.1. GGF100k

At this time, Global Geomagnetic Field over the past 100 ka (GGF100k, Panovska et al. (2018)) is the longest time-varying PFM encompassing times with multiple excursions to include Hilina Pali, Mono-Lake/Auckland, Laschamp, Norwegian-Greenland Sea, and Post Blake. It incorporates over 100 sediment records (Fig. 1a) and does not impose any regional stacking of the originally published records. The model uses a smoothing kernel or a temporal filter in the forward model, which modifies the model prediction to account for the variable temporal resolution of each sediment record. This allows the model to accommodate expected variations in fitting the data based on each record's sedimentation rate. The B-spline knot spacing is 200 years, and the maximum SH degree and order is ten. Not all the listed excursions are visible in this model, either because they are regional events or as a result of various constructive choices.

2.2. GGFSS70

A more recent model is GGFSS70, the Global Geomagnetic Field model spanning 70–15 ka (Panovska et al., 2021). It covers Mono-Lake/Auckland, Laschamp, and Norwegian-Greenland Sea excursions. It is based on nine high-resolution and well-dated sediment records (Fig. 1b). This model is the most stringent in sediment record selection and does not impose additional regional stacking or use a smoothing kernel. The B-spline knot spacing is 50 years, and the SH degree and order is limited to six.

2.3. LSMOD.2

The Laschamp model (LSMOD.2, Korte et al. (2019)) is the shortest of the three models, spanning 50–30 ka, which includes Mono Lake/Auckland and Laschamp excursions. LSMOD.2 combines regional sediment records (Fig. 1c light green circles) with similar signals to create 12 principal sediment records (dark green circles). This model does not use a smoothing kernel and selects regional sediment records to stack. The B-spline knot spacing is 50 years, and the maximum SH degree and order is ten.

2.4. Spatial and temporal resolutions

The expected differences in spatial resolution across the three models are evident from the sediment record locations from 50 to 30 ka in Fig. 1 and the time average of the spatial power spectrum in Fig. 2a. All the models share six sediment records (stars). A detailed comparison of the shared and excluded sediment records is provided in the Supplementary Section 1.1. GGFSS70 and LSMOD.2 have almost no coverage of the Pacific Ocean, and GGF100k has only sparse coverage of the eastern Pacific. The southern hemisphere has fewer data for all the models than the northern hemisphere. The contrasts in data distribution are also revealed in the spatial power spectrum, Fig. 2a, where all three models start to fall off after degree and order 4, with GGFSS70 losing power most rapidly.

Another factor to take into account when comparing PFMs is the number of SH coefficients recovered from a limited set of observations. GGF100k and LSMOD.2 are truncated at degree and order 10, yielding 120 coefficients ($l_{max}(l_{max}+2)$) where l is degree), while GGFSS70 is truncated at l=6, yielding 48 coefficients. GGF100k is based on over 100 sediment records, while LSMOD.2 and GGFSS70 use only 12 and 9 sediment records, respectively. Considering the number of free parameters, LSMOD.2 and GGFSS70 may only be capable of recovering degree and order 2 before regularization effects become predominant. Addi-

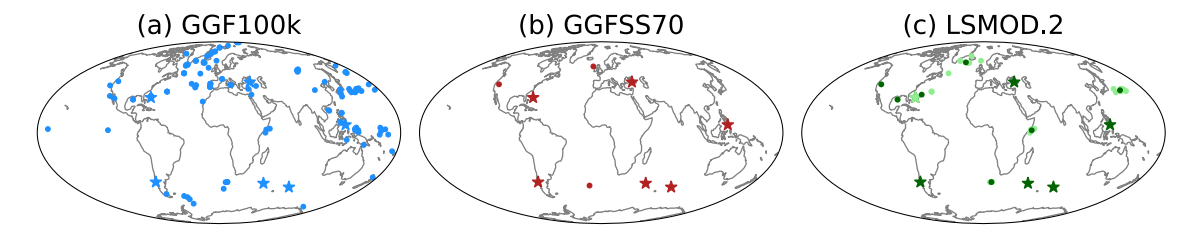


Fig. 1. Paleomagnetic sediment records from 50 to 30 ka for GGF100k (a), GGFSS70 (b), and LSMOD.2 (c). Stars are the six sediment records used in all models. Circles are individual sediment records. LSMOD.2 dark green circles are the principal stack records, and the light green circles are adjacent records contributing to each principal stack. (For interpretation of the references to colour in this figure legend, the reader is referred to the web version of this article.)

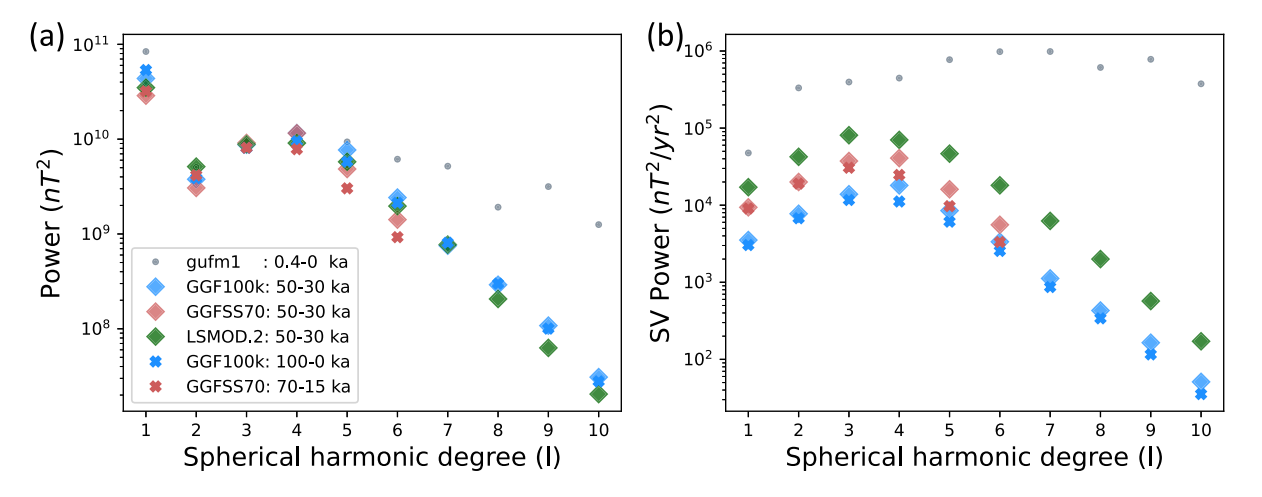


Fig. 2. Time-average of both spatial power spectrum (a) and its secular variation (b) at the CMB for GGF100k (blue), GGFSS70 (coral), LSMOD.2 (green), and gufm1 (gray). (For interpretation of the references to colour in this figure legend, the reader is referred to the web version of this article.)

tionally, the spatial coverage suggests SH degree 2 can be influenced by the lack of data in the Pacific and southern hemispheres. In spite of this, regions with reasonable data coverage could still be considered suitable for analysis.

The quantity of observations varies over the duration of each model. This is seen in the figures presented by Panovska et al. (2018), Fig. 1b) and Panovska et al. (2021), Fig. 1b) for GGF100k and GGFSS70. In the case of GGF100k, there is a gradual decline in data observations farther back in time. For GGFSS70, there is an increase in data around 58 ka, 44 to 33 ka, and 23 ka, and a decrease in data from 22 to 15 ka. The number of observations as a function of time has not been shown for LSMOD.2.

The temporal resolutions differ based on constructive choices and sediment rates. Differences in temporal resolution are seen in Fig. 2b in the time averages of power in the secular variation. GGF100k is the smoothest model with the lowest power in secular variation across all SH degrees. LSMOD.2 has the highest apparent temporal resolution across all SH degrees. GGFSS70 has an intermediate temporal resolution, lower than LSMOD.2 but higher than GGF100k. The time averages of secular variation for GGF100k and GGFSS70 have slightly more power during the common period of 50–30 ka (diamonds) compared to each model's total duration; this is expected since the common period has higher secular variation during the Laschamp and Mono Lake/ Auckland excursions. There are clear differences across the power spectra of the three models, so we should expect contrasting results.

3. Methods

In this section, we illustrate our methods using a complete and robust SH representation provided by a numerical dynamo simulation, LEDT002 (Nakagawa and Davies, 2022), to highlight what we might expect from such an analysis in a perfect reproduction of field behavior. Truncating SH degrees and orders at ranges from 1 to 6 (see Supplementary Section 1.2) show the drift signal might be recovered by about

degree and order 4, where the PFMs start to lose spatial power (Fig. 2). Details about LEDT002 and a list of parameters employed in the simulation are given in Supplementary Section 1.2. Sections 3.1 and 3.2 below give the details about processing LEDT002: these differ only slightly from the methodology for PFMs which is described in Section 3.3

3.1. Time-longitude plots

To study zonal motion, we used time-longitude (TL) plots (Dumberry and Finlay, 2007; Finlay and Jackson, 2003; Nilsson et al., 2020) in which the temporal evolution of the radial field at a specific latitude (or a processed version of it designated by the subscript _p) is plotted as a function of longitude. The TL plots of the processed radial field enhance the signatures of zonal motion by removing the time-average axisymmetric components of the field (Gauss coefficients m=0). Fig. 3a shows the processed version LEDT002_p TL plot, where the time units on the vertical axis plot are given in magnetic diffusion time (t_d). Spherical harmonic degree and order up to ten were used to calculate the radial component of the field (B_r) at the CMB. We highlight examples of zonal motion in the processed TL plot for LEDT002 in Fig. 3a using dashed lines; the features are banding of magnetic flux migrating both westward (pink dashed lines) and eastward (blue dashed lines).

3.2. Spatial and temporal Radon drift assessment

We used a Radon transform (Deans, 1983) on the time-longitude plots to quantitatively estimate drift rates for which there are coherent zonal drift signals (Dumberry and Finlay, 2007; Finlay and Jackson, 2003; Nilsson et al., 2020). An illustration of the Radon transform of a time-longitude is given in the Supplementary Section 1.3. The Radon drift rate power (RDRP) determination integrates the magnetic flux of the TL plot along various angles. The angles are directly converted to the

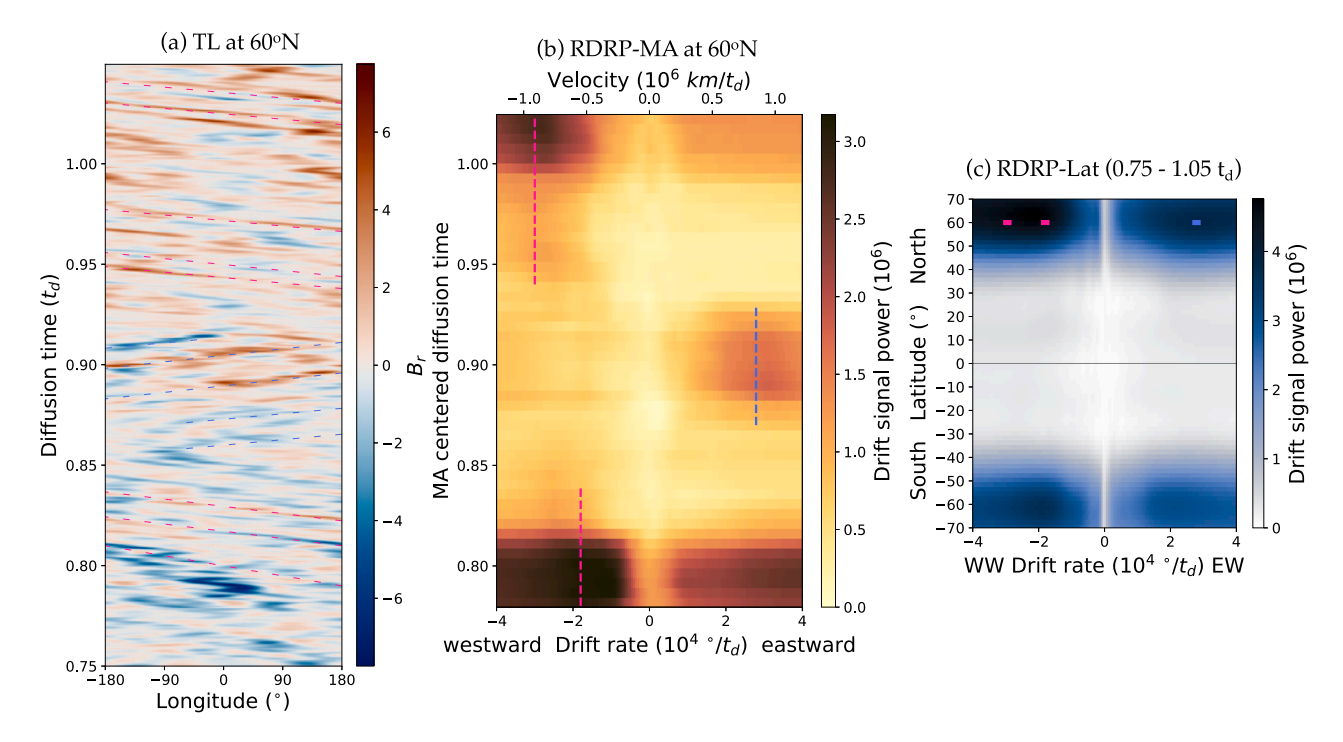


Fig. 3. LEDT002_p: (a) Time-longitude of the processed radial field at the CMB ($60^{\circ}N$) from 0.75 to 1.05 t_d . Time-longitude plot has a longitudinal spacing of 2° and 0.0005 t_d . The time-average axisymmetric parts of the field were removed. (b) RDRP moving average in time (RDRP–MA). A 0.05 t_d window with 0.005 t_d increments was used at each time step. (c) RDRP as a function of latitude (RDRP–Lat) with 2° latitudinal spacing. The pink and blue dashed lines highlight westward and eastward drift, respectively. (For interpretation of the references to colour in this figure legend, the reader is referred to the web version of this article.)

drift rate; shallow and steeper angles correspond to faster and slower drift rates, respectively. In Fig. 3(a), the pink and blue lines in the LEDT002_p TL plot are examples of integration lines at varying drift rate angles and correspond to the dashed lines in 3(b) which shows RDRP as a function of time localized to 60°N. In 3(c), a global perspective is provided with the time average of the RDRP plotted as a function of latitude.

The results in Fig. 3b are from a RDRP moving average in time (RDRP-MA) of the LEDT002_p TL plot with a window length of 0.05 t_d at 0.005 t_d steps to show the drift rate variability throughout time. The LEDT002_p RDRP-MA shows the corresponding drift rates changing from the pink westward drift to the blue eastward drift and then returning to the pink westward drift. Nilsson et al. (2020)(Fig. 2b) had a similar figure that was renormalized at each time step. We refrained from renormalizing to preserve the changes in power evident over time.

The global view of Radon drift provided by a RDRP time average as a function of latitude (RDRP-Lat) for LEDT002_p in Fig. 3c shows the geographical drift rate distribution. RDRP-Lat was created by calculating TL plots at latitudes from 70° N to 70° S with 2° latitudinal spacing and performing an RDRP calculation over the specified time intervals (here 0.75–1.05 t_d). The pink and blue drift rates from (a) are also highlighted at 60° N in Fig. 3c. Our RDRP-Lat uses the same methodology as for Holocene models by Nilsson et al. (2020)(Fig. 2a) and Dumberry and Finlay (2007)(Fig. 2). Dumberry and Finlay (2007) called these plots latitude–azimuthal speed power (LASP).

3.3. Methods for paleomagnetic field models

The PFMs differ from our sample of the LEDT002 numerical simulation in having quasi-stationary features. To emphasize zonal drift, it is essential to eliminate these features from the PFMs. The processed TL, RDRP–MA, and RDRP–Lat plots for PFMs undergo the same methods as LEDT002_p as described above. However, an additional step involves the removal of quasi-stationary features using a high-pass Butterworth filter with a cutoff at a 4000-year period ($f_c = 0.00025/yr$), a step not

applied to the numerical simulation. Longer period (i.e., slower) drift rates will not be detected in RDRP–MA and RDRP–Lat. We chose a 4000-year cutoff period to balance removing quasi-stationary features and capturing adequate drift signals from the original field. For GGF100k, we captured approximately 40% of the residual field from the original radial field at the CMB as seen in the Supplementary Section 1.4. In Fig. S6, we show a TL plot with a cut-off period of 10,000 years in which quasi-stationary features are visible.

Spherical harmonic degree and order up to ten were used to calculate the radial component of the field (B_r) at the CMB, except for GGFSS70, for which the maximum degree and order were six. The PFMs' TL plots have a grid spacing of 2° longitude and 10-year increments. The Radon drift moving average was performed on a 4000-year window at 200-year time steps.

4. Geomagnetic results

4.1. High-latitude reverse flux patches given by time-longitude plots

Time-longitude plots of the full radial field (unprocessed) highlight the duration and strength of reverse and intense flux patches at the coremantle boundary around a latitudinal small circle. Regionally reversed/ strong flux patches are of opposite polarity/unusual strength relative to the expected field polarity/strength at that location. For instance, in the northern hemisphere today, a positive field is considered reverse and a strong negative field is considered intense. Fig. 4 shows the three PFMs' unprocessed TL plots for each model at 55°N with their time axes aligned. The tick marks above each TL plot indicate the sediment records located within $20^{\circ}N/S$ of $55^{\circ}N$. The left columns show the summation of reverse/ weak magnetic (10% of the average B_r in each TL plot) flux across all longitudes. We chose $55^{\circ}N$ latitude for the best data coverage and the location of the reverse and intense flux patches. The TL plots for the southern hemisphere are in Supplementary Section 1.5. These timelongitude plots allow us to see the high-latitude magnetic flux concentrations and successive occurrences of reversed patches for the past 100 ka.

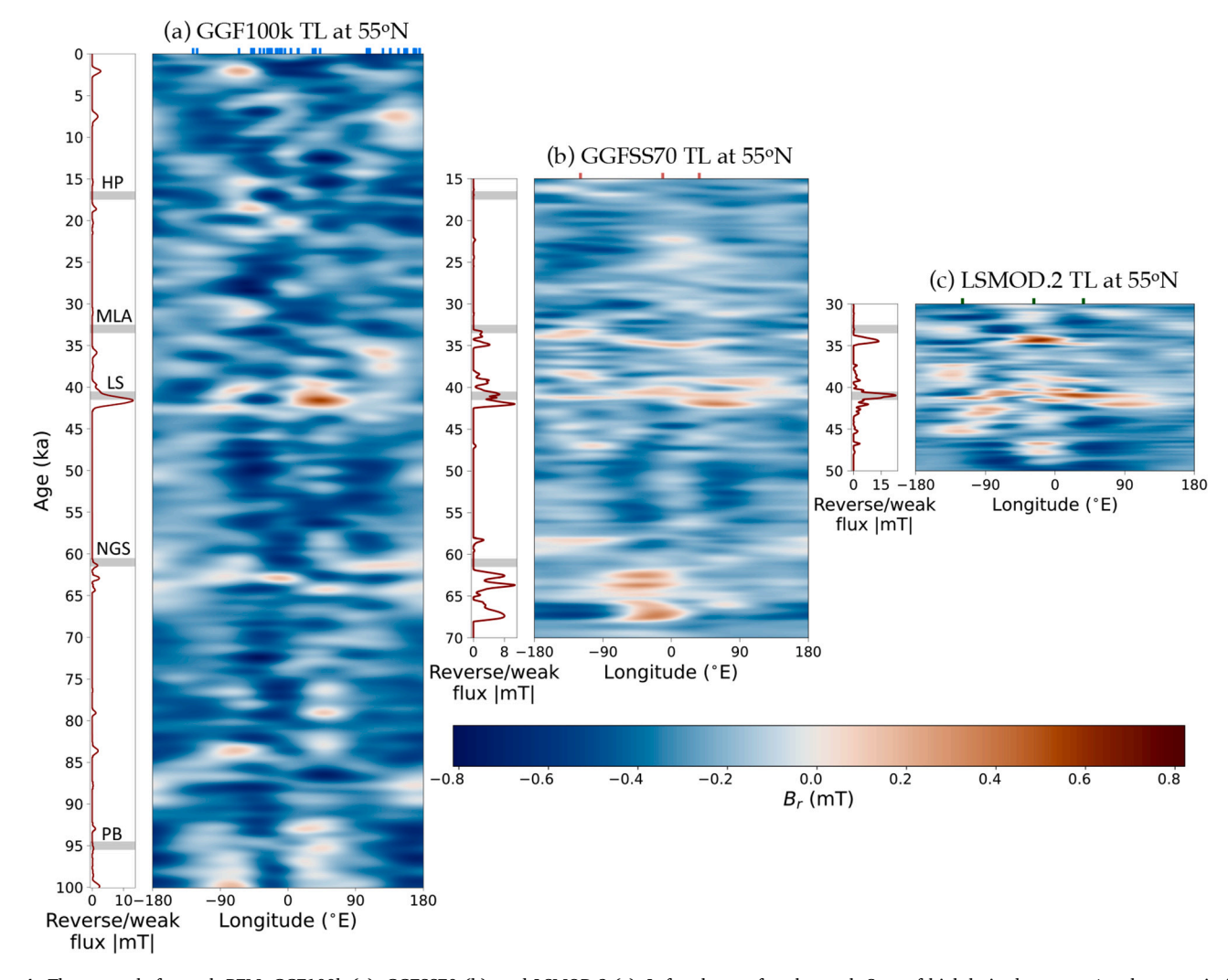


Fig. 4. Three panels for each PFM: GGF100k (a), GGFSS70 (b), and LSMOD.2 (c). Left column of each panel: Sum of high-latitude reverse/weak magnetic flux patches around the latitudinal small circle (a: $B_r > -0.031$, b: $B_r > -0.021$, c: $B_r > -0.022$ mT). The shaded gray regions show the excursions: Hilipa Pali (HP), Mono Lake/ Auckland (MLA), Laschamp (LS), Norwegian-Greenland Sea (NGS), and post-Blake (PB). Right column of each panel: Time-longitude of the full radial field at the CMB (55°N). The top tick marks correspond to the sediment records from 35°N to 75°N in Fig. 1. (For interpretation of the references to colour in this figure legend, the reader is referred to the web version of this article.)

Reverse flux patches are most prominent during excursions but also occur at other times not associated with an excursion (e.g., 10–1 ka, 90–80 ka). They are associated with weak fields and appear to have an 8–20 kyr occurrence throughout all models. During the Mono-Lake/Auckland excursion, GGFSS70 and LSMOD.2 have reverse flux patches that occur at different locations. In contrast, GGF100k does not seem to display prominent reverse flux patches at that time. The relative power levels and resolution for the three models in the secular variation plots of Fig. 2b are also reflected in the TL figures with GGF100k being the smoothest and LSMOD.2 having the highest apparent temporal variability.

The geographical magnetic flux concentrations (reverse and intense) vary across all models, but this is expected given the differences in contributory data and temporal resolution. GGF100k has reverse flux concentrations around $90^{o}W$ and $50^{o}E$ and intense flux patches generally in the Atlantic region ($0^{o}-90^{o}W$). GGFSS70 has reverse flux concentrated at 0^{o} , followed by $130^{o}W$ and $130^{o}E$. LSMOD.2 has reverse flux concentrations in the Atlantic hemisphere with a center at $30^{o}W$ and intense flux concentrations in the western Atlantic at $60^{o}W$ and eastern Europe at $45^{o}E$. The strongest magnetic flux concentrations do not appear in the Pacific hemisphere ($150^{o}E-120^{o}W$) where data coverage is wanting, particularly with GGFSS70 and LSMOD.2. The

magnetic flux concentrations appear to exhibit greater detail near sediment records as indicated by the tick marks above each TL plot. The most prominent reverse flux patches are during the Laschamp excursion, with varying spatial resolutions and geographical distributions across all models. GGFSS70 has more pronounced Norwegian-Greenland Sea ($\sim\!61$ ka) and Mono Lake/Auckland ($\sim\!33$ ka) excursion signatures than GGF100k. Although there are differences (e.g., geographical, duration, intensity) in the reverse and intense flux patches, the characteristic features occur across all three models. Next, we will use the Radon drift analysis to assess the drift rate of the magnetic flux concentrations for the past 100 ka.

4.2. High-latitude zonal drift

We used the RDRP-MA to quantitatively estimate the changes in the rate and strength of zonal drift of magnetic flux concentrations. Colored panels in Figs. 5 and 6 show the RDRP-MA for $55^\circ N$ and $55^\circ S$, respectively, for the three models. Within each panel, the figures also contain the maximum drift signal (middle column), dipole tilt (black line in the left column), and axial dipole moment (red line in the left column). These plots provide a clearer view of the dominant drift signal power and drift rate for the past 100 ka.

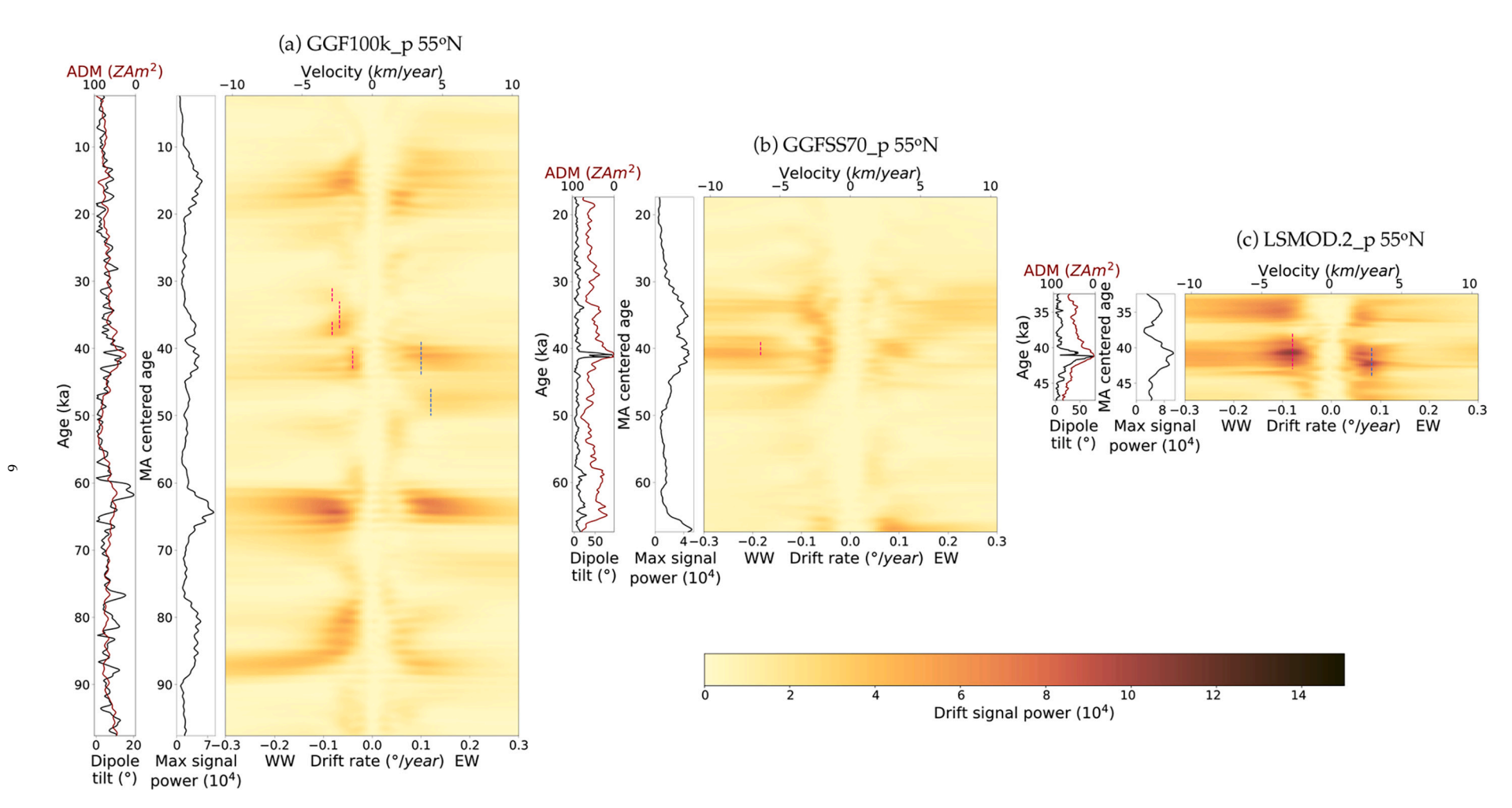


Fig. 5. Northern hemisphere RDRP moving average in time for GGF100k_p (panel a), GGFSS70_p (panel b), and LSMOD.2 (panel c) at 55°N. Left columns of each panel: dipole tilt (black) and axial dipole moment (dark red). ADM axis is reversed. Middle columns of each panel: maximum signal power. Right columns of each panel: model_p RDRP-MA. A 4000-year window with 200-year increments was used at each time step. The drift rates near zero are cut by the high-pass filter. The pink and blue dashed lines correspond to the westward and eastward drift in Fig. 7. Note that we have chosen to preserve a single scale across all colour contour plots, leading to under-saturation in (b) and over-saturation in Fig. 6(b). A precise reflection of the magnitude of drift signals can be found from the maximum signal power. (For interpretation of the references to colour in this figure legend, the reader is referred to the web version of this article.)

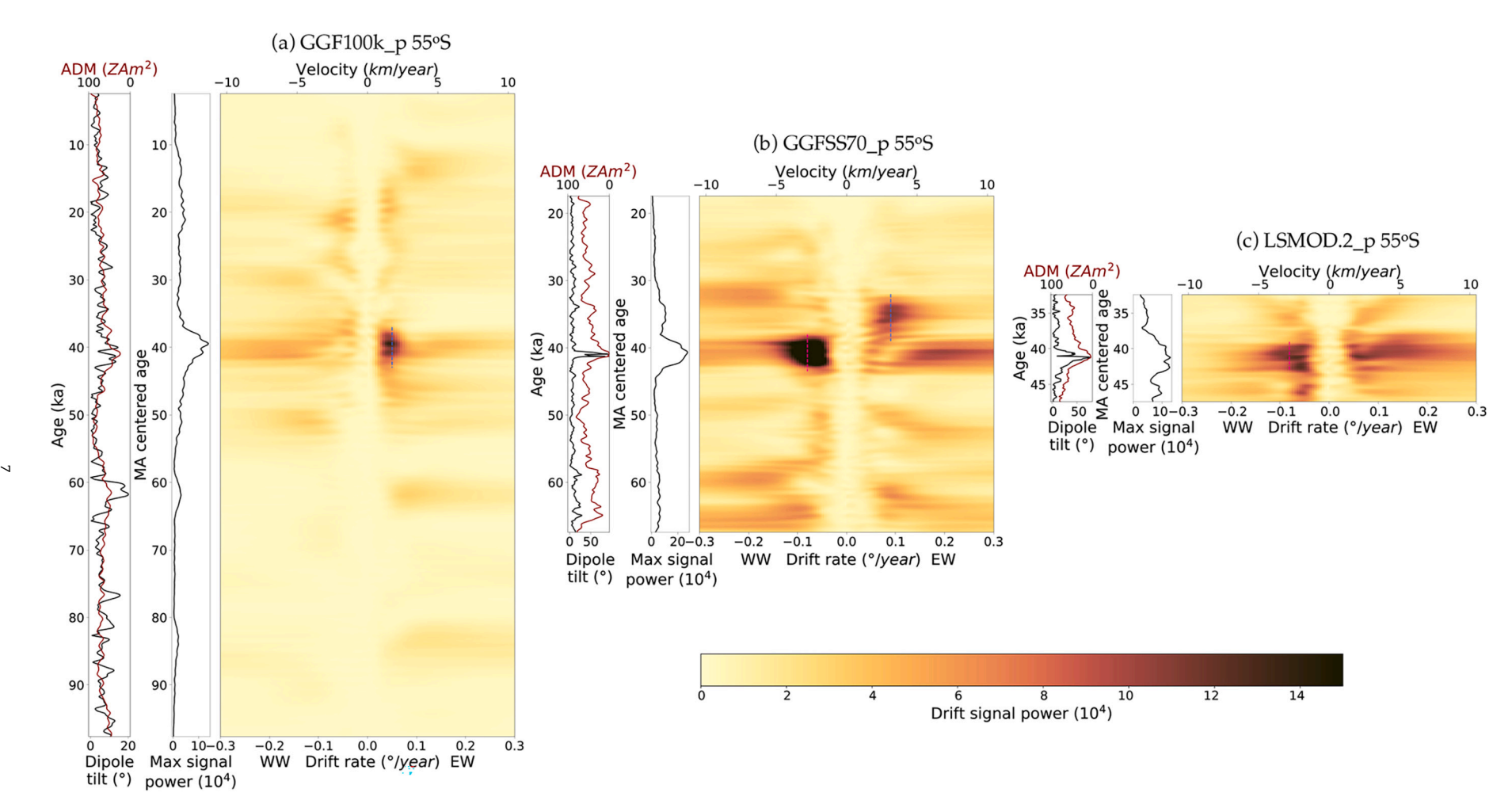


Fig. 6. Southern hemisphere RDRP moving average in time for GGF100k_p (panel a), GGFSS70_p (panel b), and LSMOD.2 (panel c) at 55°S. Left columns of each panel: dipole tilt (black) and axial dipole moment (dark red). ADM axis is reversed. Middle columns of each panel: maximum signal power. Right columns of each panel: model_p RDRP-MA. A 4000-year window with 200-year increments was used at each time step. The drift rates near zero are cut by the high-pass filter. The pink and blue dashed lines correspond to the westward and eastward drift in Fig. 7. Note that we have chosen to preserve a single scale across all colour contour plots, leading to under-saturation in Fig. 5(b) and over-saturation in (b). A precise reflection of the magnitude of drift signals can be found from the maximum signal power. (For interpretation of the references to colour in this figure legend, the reader is referred to the web version of this article.)

In the northern hemisphere (Fig. 5), there are recurrent eastward and westward drift episodes; the episodes of maximum power in the drift signal coincide with the five excursions (Hilina Pali (\sim 17 ka), Mono Lake/ Auckland (\sim 33 ka), Laschamp (\sim 41 ka), Norwegian-Greenland Sea (\sim 61 ka), post-Blake (\sim 95 ka) (Laj and Channell, 2015, p. 345–356)) but also occur during a quiet period from 86 to 80 ka where there is no evidence for any excursion. Eastward and westward drift episodes co-occur in each model, particularly during the Laschamp excursion. LSMOD.2_p has the strongest RDRP compared to GGF100k_p and GGFSS70_p; the difference could be from the temporal resolution of each model. Generally, in the northern hemisphere, westward drift dominates in occurrence and drift signal power.

In the southern hemisphere (Fig. 6), the drift signal for the past 100 ka is strongest during the Laschamp excursion across all models. GGF100k_p has a dominant eastward drift signal, while GGFSS70_p and LSMOD.2 p have a mixture of westward and eastward drift signals.

The northern and southern hemispheres' drift signals are not coherent in time but have a common drift rate range of $\pm 0.05^0/\mathrm{yr}$ to $\pm 0.18^o/\mathrm{yr}$. GGFSS70_p and LSMOD.2_p have similar drift rates that are distinct from GGF100k_p, which is expected since GGF100k_p is smoother and there is smearing of the faster drift rates. The maximum drift signals correlate with a weak axial dipole moment and a high dipole tilt. The maximum drift signals also coincide with the weak field and reverse flux patches in Fig. 4. Next, we will focus on the interval 50–30 ka and look at the processed time-longitude plots at high latitudes.

4.3. High-latitude zonal motion for 50-30 ka

We use time-longitude plots of processed models to track the zonal motion of magnetic flux concentrations, intense and reverse flux patches, in B_r at the CMB around a latitudinal small circle. In this section, we focus on the interval 50–30 ka where all three models overlap in time and which, most importantly, contains the Laschamp excursion (\sim 41 ka) producing the drift signal indicated by the pink and blue dashed lines in Figs. 5 and 6. Fig. 7 shows the TL plots for all three processed models at 55°N (top row) and 55°S (bottom row). The tick marks above each processed TL plot indicate locations of the sediment records within $20^{\circ}N/S$ of 55°N. The blue dashed lines highlight eastward drift, and the pink dashed line highlights westward drift. The drift rates are not distinct but rather a range of velocities, as seen in the RDRP-MA (Figs. 5 and 6).

An eastward-to-westward transition in the northern hemisphere seems to occur during the Laschamp excursion (gray dashed line). Zonal migration of the flux patches is best seen in GGF100k_p TL (55°N) with eastward (blue dashed line) motion preceding the Laschamp excursion and then transitioning westward (pink dashed line). GGFSS70_p and LSMOD.2_p exhibit a similar eastward-to-westward transition, but both models have constructive choices limiting the signature of zonal motion. GGFSS70 spatial coverage is restricted to the Atlantic hemisphere, and LSMOD.2 has patchier magnetic flux concentrations, possibly due to the stacking of sediment records.

In the southern hemisphere, there is no consensus across the models except for GGFSS70_p and LSMOD.2_p having strong magnetic flux concentrations migrating westward during the Laschamp excursion (pink dashed lines in Fig. 7(e,f)). These magnetic flux concentrations are the dominating westward drift signal found in Fig. 6(b,c). The reverse (blue) flux patch peaks at $90^{\circ}W$ in Fig. 7e, near the location of the offshore Chile site (farthest left tick mark), ODP 1233 (Lund et al., 2006b,Lund et al., 2006a). This site provides the westernmost sediment record, representing the South Pacific for all models. GGFSS70_p and LSMOD.2_p southern drift signals are strongly influenced by the data distribution of the four southern sediment records, particularly ODP 1233. GGF100k has several more sediment records in the South Atlantic and Southwestern Pacific than either GGFSS70 or LSMOD.2. In GGFSS70_p, the reverse flux patches transition eastward at \sim 39 ka. The westward-to-eastward transition is not as clearly seen in LSMOD.2_p.

Within each model, the high-latitude signals are not coherent between the northern and southern hemispheres, possibly indicating no simple global pattern of zonal motion. In the next section, we confirm this by extending our analysis beyond the latitudes of $55^{\circ}N$ and $55^{\circ}S$ and assessing global zonal drift.

4.4. Global drift for 50-30 ka

Continuing our focus on the $50{\text -}30$ ka time interval, we show the global drift distribution with the RDRP time average as a function of latitude from $70^\circ N$ to $70^\circ S$ (designated RDRP-Lat) in Fig. 8. During this period, the strongest drift signals occur in the southern hemisphere, which is consistent with the RDRP-MA plots in sections 4.2 and 4.3. In the region $40^\circ S$ to $65^\circ S$, GGFSS70_p and LSMOD.2_p have dominant westward drift centered at $-0.07^\circ/\text{yr}$ (WW), but GGF100k_p has dominant eastward drift at the same latitudes centered at $0.05^\circ/\text{yr}$ (EW). In the previous section, we showed the magnetic flux concentrations creating the differing drift signals across the models. We are not surprised by these contrasting results because of the constructive choices, particularly the data distribution in the southern hemisphere.

The analysis of Fig. 8 also shows that drift signals are latitudinally localized, and the northern and southern hemispheres are not symmetric. Despite equatorial drift being prominent in the modern field, it is not an important feature in the PFMs. Mid-latitude drift rates range from $-0.06^{\rm o}/{\rm yr}$ to $-0.12^{\rm o}/{\rm yr}$ (WW) and $0.05^{\rm o}/{\rm yr}$ to $0.08^{\rm o}/{\rm yr}$ (EW). At high northern latitudes, LSMOD.2 has both eastward and westward drift signals; the magnetic flux concentrations seen in Fig. 7c show zonal motion in both directions. On the other hand, the GGFSS70_p drift signal is weakly westward. GGF100k_p has both drift directions, with westward being more dominant; this arises from an eastward-to-westward transition occurring during the Laschamp excursion.

4.5. Global drift for 90-80 ka

In the previous two sections, we focused on the period 50-30 ka, which highlighted the zonal drift associated with the Laschamp excursion; however, the period 90-80 ka also has strong high-latitude drift signals that are not associated with an excursion. In Fig. 9a, we show the global drift distribution with RDRP-Lat accompanied by four separate time-longitude plots of processed models at 55°N(b), 55°S(c), 20°N(d), and 20°S(e). Fig. 9a again shows the drift signals in the northern and southern hemispheres are not symmetric. This could be from the disparate data distributions in the northern and southern hemispheres, as indicated by the tick marks. For GGF100k p, the TL plot at 55°N (b) shows the magnetic flux concentrations migrating westward in the Atlantic and eastward in the Pacific hemispheres. At a high latitude in the southern hemisphere, 55°S, the GGF100k p TL (c) shows eastward motion from Chile to the mid-Indian Ocean (90° W-80° E) but washes out beyond that boundary. The strong drift signal at mid-northern latitudes, $20^{\circ}N(d)$, is not evident at $20^{\circ}S(e)$. $20^{\circ}N$ is unique because it has full data coverage around the latitudinal small circle. The magnetic flux concentrations converge toward the Atlantic Ocean, moving eastward from the eastern Pacific and westward from the western Pacific. During this period, the dipole tilt (Fig. 5a) has a bit more variation than might be expected for a quiet period. We are limited in our analysis for this period due to GGF100k being the only model extending to 100 ka. Another period of interest that is covered by GGF100k and GGFSS70 and includes the Norwegian-Greenland Sea excursion is 70-50 ka, and we included similar plots in the Supplementary Section 1.6.

5. Discussion

5.1. Data distribution & model comparison

The constructive choices of the PFMs influence our results. The data distribution and data selection (Fig. 1) is the most significant factor

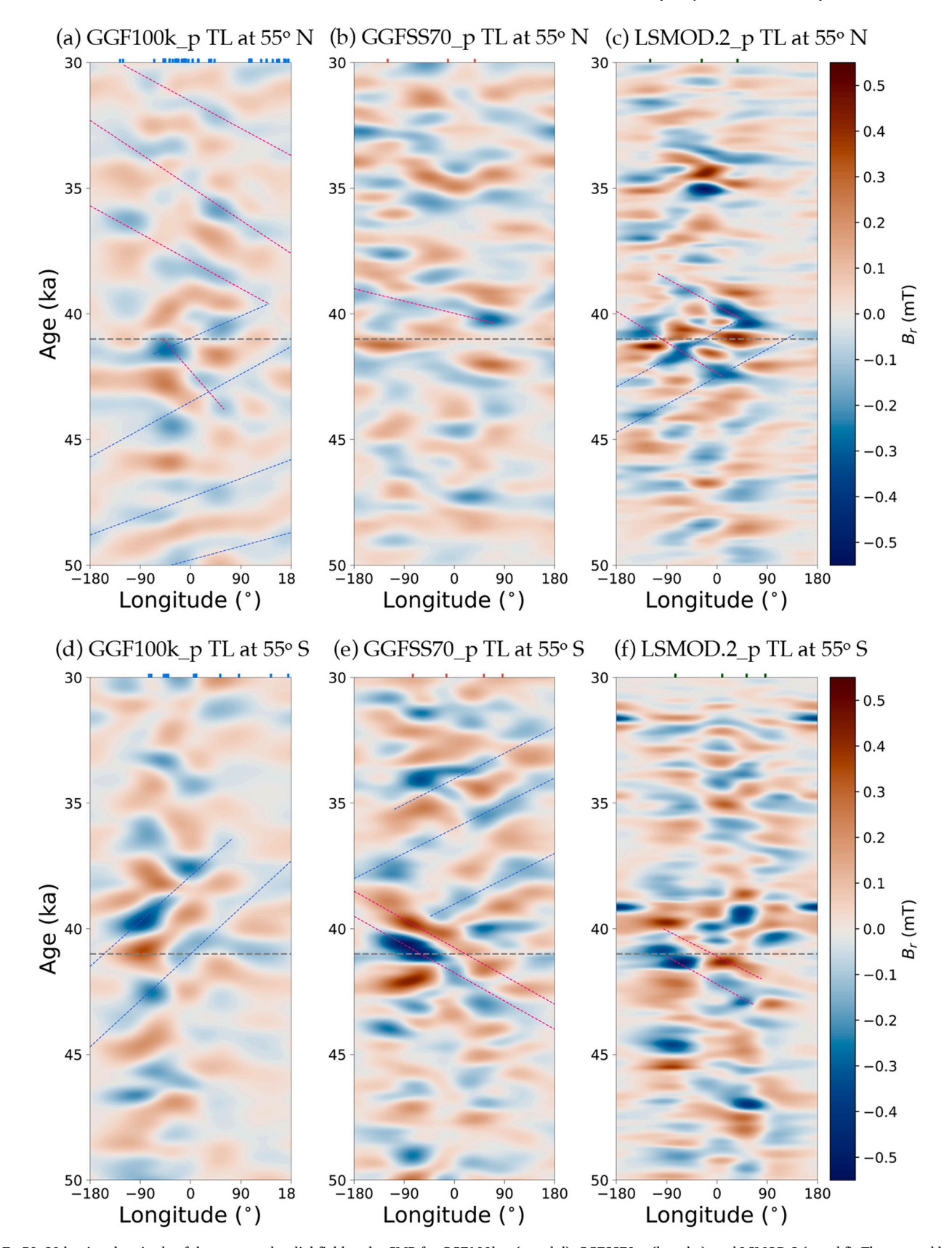


Fig. 7. 50–30 ka time-longitude of the processed radial field at the CMB for GGF100k_p (a and d), GGFSS70_p (b and e), and LSMOD.2 (c and f). The top and bottom rows are $55^{\circ}N$ and $55^{\circ}S$ latitudes, respectively. The top tick marks show the sediment records within 20° north or south of each time-longitude plot. Gray dashed line marks the Laschamp excursion. The blue and pink dashed lines express magnetic flux concentrations' eastward and westward zonal motion, respectively. The time-average axisymmetric part of the field was removed and high passed ($f_c = \frac{1}{4000 \, years}$) with a Butterworth filter. (For interpretation of the references to colour in this figure legend, the reader is referred to the web version of this article.)

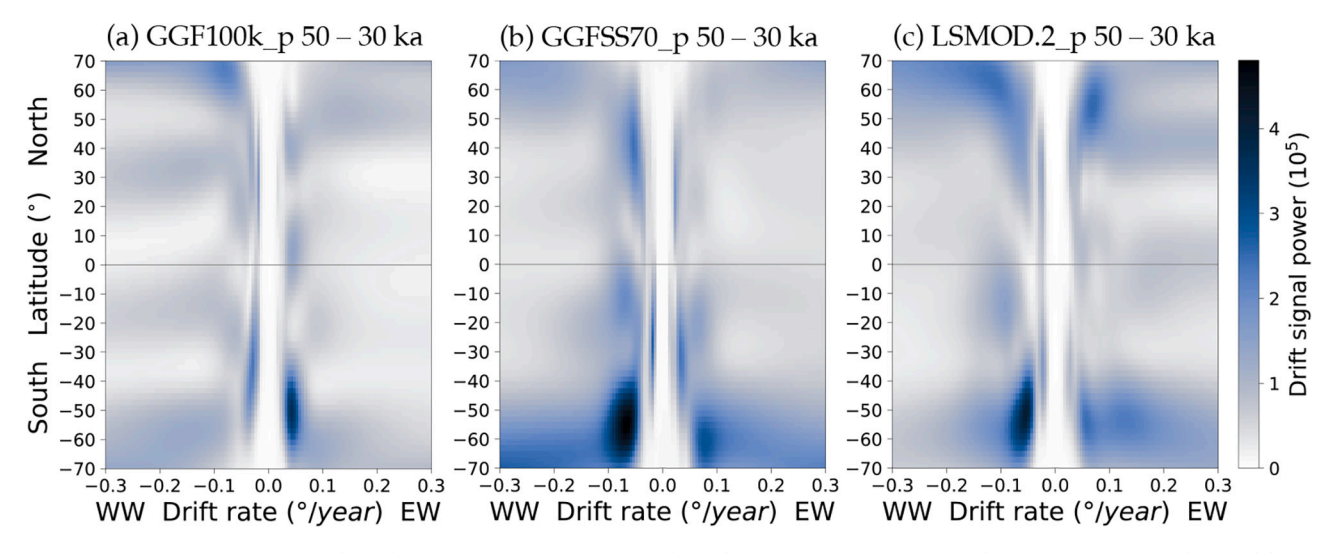


Fig. 8. RDRP time average as a function of latitude for GGF100_p (a), GGFSS70_p (b), and LSMOD.2_p (c) from 50 to 30 ka. RDRP was performed on model_p TL plots at 2° latitude spacing. The drift rates near zero are filtered out with high-pass.

contributing to the differences in our Radon drift signal. With the three PFMs, we have GGF100k that uses all viable sediment records to give decent spatial coverage with the essential need for smoothing kernels in the forward model and heavy regularization in inversion, the latter contributing to a smoother model. On the opposite end of constructive choices, we have GGFSS70, which only uses nine well-dated and high-resolution sediment records giving low spatial power in the higher SH degrees (Fig. 2). LSMOD.2 balances the regional sediment record differences by compiling 12 principal records; this allows LSMOD.2 to be on par with GGF100k in terms of spatial power and have the highest temporal resolution. The PFMs' spatial power spectra, which are comparable to gufm1 (Jackson et al., 2000) up to degree and order 3–4, are enough to capture the geometry of large-scale reverse and intense flux patches.

In the southern hemisphere, the sediment records are sparse and mostly located in the South Atlantic and Indian Oceans. All PFMs share three sediment records in the southern hemisphere (details in Supplementary Section 1.1). GGFSS70 and LSMOD.2 have four sediment records in the southern hemisphere, while GGF100k has more sediment records and extends to the eastern Pacific. The three shared records dominate the drift signal in GGFSS70 and LSMOD.2; this is highlighted by the magnetic flux concentrations in Fig. 7e-f migrating westward from 44 to 40 ka but not in GGF100k (Fig. 7d). The influence of the three shared sediment records in the southern hemisphere is also exposed by RDRP-Lat (Fig. 8b,c) with GGFSS70 and LSMOD.2 having dominant westward drift. Since GGF100k contains more sediment records, this can explain the dominant eastward drift in the same latitudinal region and duration as GGFSS70 and LSMOD.2.

The South Atlantic region has the strongest magnetic flux concentrations (Fig. 7d-f) and therefore gives the strongest drift signals. The one shared sediment record, offshore Chile ODP 1233 (Lund et al., 2006a, 2006b), significantly impacts the PFMs and drift signal by influencing the entire Southern Pacific region. The data kernels of GGF100k (Fig. 1c of Panovska et al., 2018) and sample distribution of GGFSS70 (Fig. 1a of Panovska et al., 2021) show the influence of the record from ODP 1233 in both models. The westward motion of the South American magnetic flux concentrations in GGFSS70 and LSMOD.2 (Fig. 7d-f) dominates the global drift signal.

All the models have the densest data coverage in the northern hemisphere on the Atlantic side. LSMOD.2 and GGFSS70 lack Pacific coverage, more than a quarter of the Earth's surface. The TL plots, Fig. 4, for the northern hemisphere have the greatest detail of reverse and intense flux patches for longitudes from 90°W to 90°E. In addition, the eastward-to-westward drift transition at high northern latitude during

the Laschamp excursion is detected in all PFMs' RDRP-MA (Figs. 5) with phase shifts and varying geometry of the magnetic flux concentrations (Fig. 7a-c). LSMOD.2 uses only 12 principal records, intensifying the magnetic flux concentrations and influencing the drift signal. GGF100k and GGFSS70 have comparable magnetic flux strength and geometry.

We found a difference in the northern and southern hemispheres' zonal motion of magnetic flux concentrations. It might be tempting to suppose that these differences confirm previous observations from satellite and paleomagnetic studies that highlight asymmetries between the high-latitude northern and southern hemispheres. For example, Finlay et al. (2012) observes strong secular variation at high latitudes in the northern hemisphere, which is not reflected in the southern hemisphere. In the Holocene epoch, Constable et al. (2016) found higher secular variation features in the southern hemisphere compared to the northern hemisphere. Additionally, on timescales ranging from 10^5-10^6 years, paleointensity and directional data at high latitudes suggest hemispheric asymmetries (Cromwell et al., 2013) with the greatest stability in the northern hemisphere. Nevertheless, we need to acknowledge that poor data coverage limits our ability to detect hemispheric asymmetry of zonal motion.

The differences in the PFMs' handling of regional sediment rate differences and age uncertainty influence the temporal resolution. GGF100k is significantly smoother than LSMOD.2 and GGFSS70; actually, this smoothness allows the zonal motion to be more visible in the GGF100k_p TL plot (Fig. 7a,d). There is potential for filtering out the high-frequency zonal motion in GGF100k, likely from the regularization of modeling. However, GGFSS70 and LSMOD.2, with higher time-average secular variation spatial power, have similar drift rate signals. The differences across these models expose the sensitivity of the analysis but confirm the basic findings.

5.2. Zonal drift for the past 100 ka

Using the three paleomagnetic field models, we have shown the recurrence of eastward and westward drift episodes over the past 100 kyrs. First, we noted the existence of high-latitude reverse and intense flux concentrations and linked their occurrence to periods of strong drift signals. We then focused on the time 50–30 ka and found an interesting eastward-to-westward transition during the Laschamp excursion. Dumberry and Finlay (2007) found similar directional changes in zonal motion that coincided with archaeomagnetic jerks. No matter the source of the zonal directional change of the magnetic flux patches, it is clear there is some reorganization in the core flow to produce the eastward-to-westward transition during the Laschamp excursion.

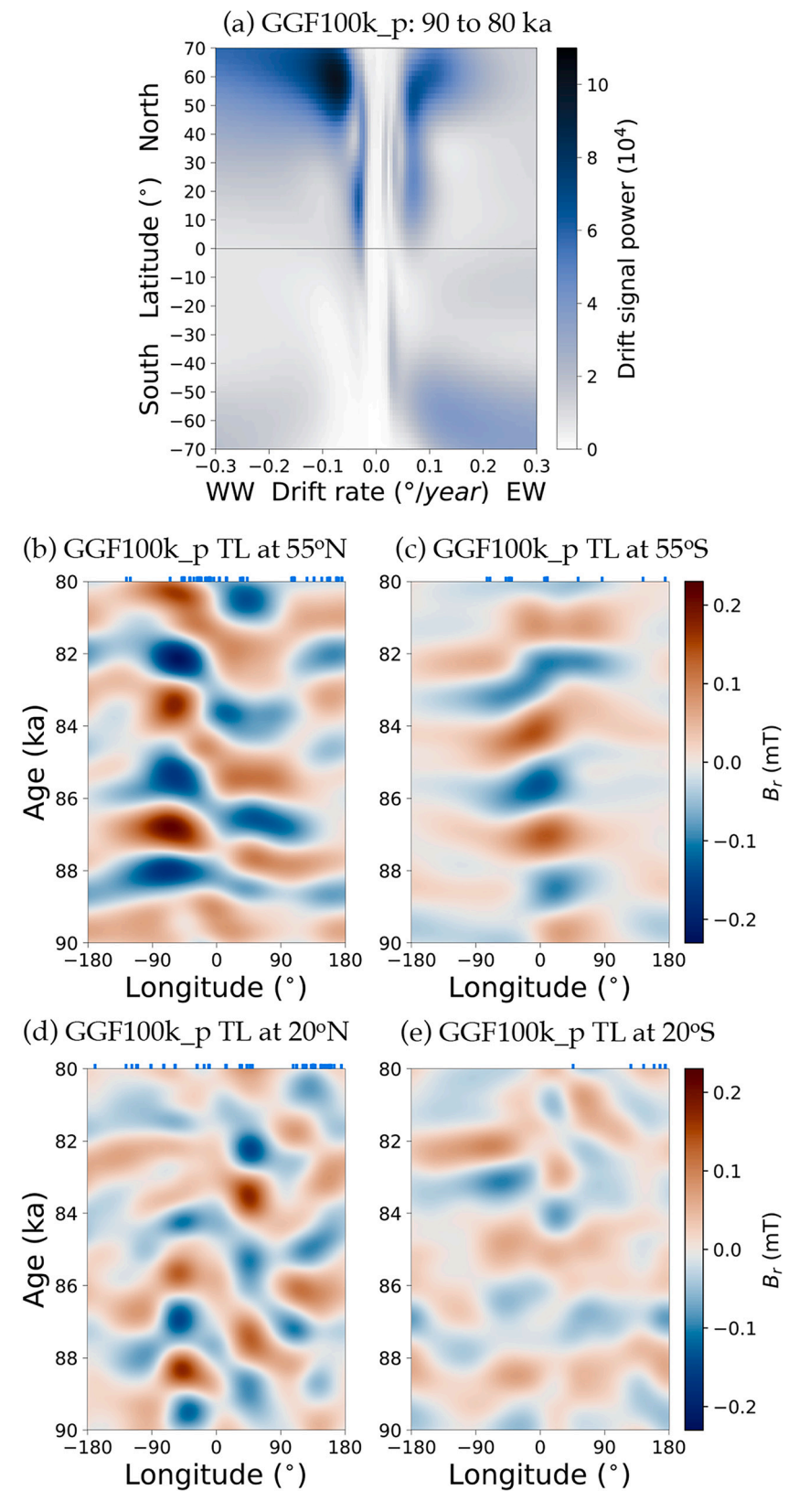


Fig. 9. GGF100k_p RDRP time average as a function of latitude (a) from 90 to 80 ka. Refer to Fig. 8 for more details on RDRP-Lat. Time-longitude of the processed radial field at the CMB for 55°N (b), 55°S (c), 20°N (d), and 20°S (e). Refer to Fig. 7 for details on GGF100k_p TL plots. The top tick marks show the longitudes of sediment records within 20° north or south of each time-longitude plot. (For interpretation of the references to colour in this figure legend, the reader is referred to the web version of this article.)

The other period we focused on was 90–80 ka since there were high latitude drift signals during a period with no excursions. We found strong mid-latitude and high-latitude drift signals in the northern hemisphere. Over the entire interval, the strongest drift signals occur when there is a decrease in the zonal to non-zonal power ratio (Z/NZ) (Fig. 23 of Panovska et al., 2019) and occasionally a decrease in the ratio of the dipole to non-axial dipole (AD/NAD). During excursions, the drift signal could be more prominent because of the exposure of non-axial dipole power; however, 90–80 ka is not associated with an excursion, and the AD/NAD has relatively low variability there.

The geodynamo processes that could potentially be the sources of eastward and westward drift are core fluid motion transporting magnetic flux (Finlay et al., 2016; Barrois et al., 2018; Livermore et al., 2017), propagation of magnetohydrodynamic waves (Hide, 1966), or a combination of both (Hori et al., 2015, 2018, 2019, 2022). The high-latitude drift we capture is possibly the zonal motion of intense and reverse flux patches. The discontinuities in the model p TL plots (Fig. 7) and possibly the RDRP-MA (Figs. 5 and 6) could also be caused by the magnetic flux concentrations migrating north or south and/or growing and decaying in place. The migration of the flux patches could be attributed to the large-scale flow transportation of gyres and jets (Finlay et al., 2016; Barrois et al., 2018; Livermore et al., 2017).

A proper discussion of the sources of westward drift would include the possibility of propagation of magnetohydrodynamic waves (Hide, 1966). The time scale of slow Rossby waves ranges from decades to multi-millennia. However, this study is not well suited for evaluating the dispersion of long-period waves: the spatial and temporal resolution limits the analysis of dispersive waves as can be seen from the Fourier wavenumber analysis in the Supplementary Section 1.7.

6. Conclusion

We have extended the tracking of zonal motion to the past 100 ka using time-varying paleomagnetic field models GGF100k, GGFSS70, and LSMOD.2. We described the benefits and drawbacks of the constructive choices of each model and the resulting temporal and spatial resolutions. GGF100k is our preferred model for assessing zonal motion using timelongitude plots because of the data distribution and the temporal and spatial smoothness. This temporal and spatial smoothness allows large-scale magnetic flux concentrations to be tracked using the Radon drift methods.

We found recurrent episodes of both eastward and westward drift, and the drift rate signals range from $\pm 0.05^{\circ}/\text{yr}$ to $\pm 0.18^{\circ}/\text{yr}$ at high latitudes; these are roughly the same as Nilsson et al. (2020); Dumberry and Finlay (2007); Bullard et al. (1950). During the Laschamp excursion in the northern hemisphere, we found an eastward-to-westward transition of the magnetic flux concentrations' zonal motion suggesting a reorganization of flow at the core surface. We see westward drift in GGFSS70 and LSMOD.2 in the southern hemisphere; however, the strong influence of ODP 1233 (Lund et al., 2006a, 2006b) and the poor southern spatial coverage hinders our interpretations. We also showed strong high-latitude and mid-latitude drift occurs in the northern hemisphere during a period with no excursions, 90-80 ka. These observations give better insight into the geodynamo processes on centennial to multi-millennial timescales. Higher spatial and temporal resolution models could potentially enhance our future insight into tracking magnetic flux movements in the paleomagnetic field.

CRediT authorship contribution statement

Nicole Clizzie: Conceptualization, Data curation, Formal analysis, Investigation, Methodology, Software, Visualization, Writing – original draft, Writing – review & editing. **Catherine Constable:** Conceptualization, Data curation, Formal analysis, Funding acquisition, Investigation, Methodology, Project administration, Resources, Software, Supervision, Validation, Visualization, Writing – original draft, Writing

- review & editing.

Declaration of competing interest

None.

Data availability

I have shared a link to my code in the manuscript.

Acknowledgements

We are grateful to Christopher Davies and Stephen Mason for providing output from the LEDT002 simulation. They also participated in invaluable discussions about our analysis, as did William Davis. We thank Brendan Reilly and Robert Hatfield for sensible conversations surrounding sedimentary data records. We acknowledge very helpful reviews from Nicolas Gillet and an anonymous reviewer. This study was supported by NSF CSEDI Grant EAR 1953778. Nicole Clizzie received support from UC San Diego's Tribal Membership Initiative Fellowship, Chief Manuelito Scholarship Program, and Veteran Affairs educational benefits (GI Bill).

Processing code for TL plots and RDRP can be found at https://github.com/clizzzie/time-longitude_and_Radon_transform.git

Appendix A. Supplementary data

Supplementary data to this article can be found online at https://doi.org/10.1016/j.pepi.2024.107143.

References

- Barrois, O., Hammer, M.D., Finlay, C.C., Martin, Y., Gillet, N., 2018. Assimilation of ground and satellite magnetic measurements: inference of core surface magnetic and velocity field changes. Geophys. J. Int. 215, 695–712. URL: https://academic.oup. com/gji/article/215/1/695/5057476 https://doi.org/10.1093/gji/ggy297.
- Bullard, E.C., Freedman, C., Gellman, H., Nixon, J., 1950. The westward drift of the Earth's magnetic field. Philos. Trans. R. Soc. Lond. 243, 67–92. https://doi.org/ 10.1098/rsta.1950.0014.
- Constable, C., Korte, M., 2015. Centennial- to millennial-scale geomagnetic field variations. In: Treatise on Geophysics. Elsevier, pp. 309–341. URL: https://linkinghub.elsevier.com/retrieve/pii/B9780444538024001032 https://doi.org/10.1016/B978-0-444-53802-4.00103-2.
- Constable, C., Korte, M., Panovska, S., 2016. Persistent high paleosecular variation activity in southern hemisphere for at least 10 000 years. Earth Planet. Sci. Lett. 453, 78–86. https://doi.org/10.1016/j.epsl.2016.08.015.
- Cromwell, G., Tauxe, L., Staudigel, H., Constable, C.G., Koppers, A.A.P., Pedersen, R., 2013. In search of long-term hemispheric asymmetry in the geomagnetic field: results from high northern latitudes. Geochem. Geophys. Geosyst. 14, 3234–3249. URL: https://agupubs.onlinelibrary.wiley.com/doi/10.1002/ggge.20174 https://doi.org/10.1002/ggge.20174.
- Deans, S.R., 1983. The Radon Transform and some of its Applications. John Wiley and Sons, New York.
- Dumberry, M., Finlay, C.C., 2007. Eastward and westward drift of the Earth's magnetic field for the last three millennia. Earth Planet. Sci. Lett. 254, 146–157. https://doi. org/10.1016/j.epsl.2006.11.026.
- Finlay, C.C., Jackson, A., 2003. Equatorially dominated magnetic field change at the surface of Earth's Core. Science 300, 2084–2086. https://doi.org/10.1126/ science.1083324.
- Finlay, C.C., Jackson, A., Gillet, N., Olsen, N., 2012. Core surface magnetic field evolution 2000-2010: Core surface magnetic field evolution. Geophys. J. Int. 189, 761–781. URL: https://academic.oup.com/gji/article-lookup/doi/10.1111/j.136 5-246X.2012.05395.x https://doi.org/10.1111/j.1365-246X.2012.05395.x.
- Finlay, C.C., Aubert, J., Gillet, N., 2016. Gyre-driven decay of the Earth's magnetic dipole. Nat. Commun. 7, 1–8. https://doi.org/10.1038/ncomms10422.
- Gallet, Y., Genevey, A., Courtillot, V., 2003. On the possible occurrence of 'archaeomagnetic jerks' in the geomagnetic field over the past three millennia. Earth Planet. Sci. Lett. 214, 237–242. URL: https://linkinghub.elsevier.com/retrieve/pii/S0012821X03003625 https://doi.org/10.1016/S0012-821X(03)00362-5.
- Gallet, Y., Hulot, G., Chulliat, A., Genevey, A., 2009. Geomagnetic field hemispheric asymmetry and archeomagnetic jerks. Earth Planet. Sci. Lett. 284, 179–186. URL: htt ps://linkinghub.elsevier.com/retrieve/pii/S0012821X09002453 https://doi.org/10 .1016/i.epsl.2009.04.028.
- Gerick, F., Jault, D., Noir, J., 2021. Fast quasi-geostrophic magneto-Coriolis modes in the Earth's Core. Geophys. Res. Lett. 48 https://doi.org/10.1029/2020GL090803.

- Gillet, N., Gerick, F., Jault, D., Schwaiger, T., Aubert, J., Istas, M., 2022. Satellite magnetic data reveal interannual waves in Earth's core. Proceed. National Acad. Sci. 119 https://doi.org/10.1073/pnas.2115258119.
- Gubbins, D., 1975. Can the Earth's magnetic field be sustained by core oscillations? Geophys. Res. Lett. 2, 409–412. URL: https://agupubs.onlinelibrary.wiley.com/doi/10.1029/GL002i009p00409 https://doi.org/10.1029/GL002i009p00409.
- Halley, E., 1683. A theory of the variation of the Magnetical compass. Philos. Trans. R. Soc. Lond. 13, 208–221. https://doi.org/10.1098/rstl.1683.0031.
- Halley, E., 1692. An account of the cause of the change of the variation of the magnetical needle. With an hypothesis of the structure of the internal parts of the earth: as it was proposed to the Royal Society in one of their late meetings. Philos. Trans. R. Soc. Lond. 17, 563–578. URL: https://royalsocietypublishing.org/doi/10.1098/rstl.1686. 0107 https://doi.org/10.1098/rstl.1686.0107.
- Hide, R., 1966. Free hydromagnetic oscillations of the Earth's core and the theory of the geomagnetic secular variation. Philos. Trans. R. Soc. Lond. 259, 615–650.
- Holme, R., 2015. Large-scale flow in the Core. In: Treatise on Geophysics. Elsevier, pp. 91–113. URL: https://linkinghub.elsevier.com/retrieve/pii/B9780444538 02400138X https://doi.org/10.1016/B978-0-444-53802-4.00138-X.
- Hori, K., Jones, C.A., Teed, R.J., 2015. Slow magnetic Rossby waves in the Earth's core. Geophys. Res. Lett. 42, 6622–6629. URL: https://onlinelibrary.wiley.com/doi/abs/1 0.1002/2015GL064733 https://doi.org/10.1002/2015GL064733.
- Hori, K., Teed, R., Jones, C., 2018. The dynamics of magnetic Rossby waves in spherical dynamo simulations: a signature of strong-field dynamos? Phys. Earth Planet. Inter. 276, 68–85. URL: https://linkinghub.elsevier.com/retrieve/pii/S0031920117300 730 https://doi.org/10.1016/j.pepi.2017.07.008.
- Hori, K., Teed, R., Jones, C., 2019. Anelastic torsional oscillations in Jupiter's metallic hydrogen region. Earth Planet. Sci. Lett. 519, 50–60. URL: https://linkinghub.else vier.com/retrieve/pii/S0012821X19302468 https://doi.org/10.1016/j.epsl.2019.0 4 042
- Hori, K., Nilsson, A., Tobias, S.M., 2022. Waves in planetary dynamos. Reviews of modern. Plasm. Phys. 7, 5. URL: https://link.springer.com/10.1007/s41614-022 -00104-1 https://doi.org/10.1007/s41614-022-00104-1.
- Jackson, A., Finlay, C., 2015. Geomagnetic secular variation and its applications to the Core. In: Treatise on Geophysics. Elsevier, pp. 137–184. URL: https://linkinghub.else vier.com/retrieve/pii/B9780444538024000993 https://doi.org/10.1016/B978-0-444-53802-4.00099-3.
- Jackson, A., Jonkers, A.R.T., Walker, M.R., 2000. Four centuries of geomagnetic secular variation from historical records. Philos. Trans. R. Soc. London, Ser. A 358, 957–990. URL: https://royalsocietypublishing.org/doi/10.1098/rsta.2000.0569 https://doi. org/10.1098/rsta.2000.0569.

- Korte, M., Constable, C.G., 2005. Continuous geomagnetic field models for the past 7 millennia: 2. CALS7K: geomagnetic field models, 2. Geochem. Geophys. Geosyst. 6 https://doi.org/10.1029/2004GC000801.
- Korte, M., Brown, M.C., Panovska, S., Wardinski, I., 2019. Robust characteristics of the Laschamp and mono Lake geomagnetic excursions: results from global field models. Front. Earth Sci. 7, 86. URL: https://www.frontiersin.org/article/10.3389/feart.20 19.00086/full https://doi.org/10.3389/feart.2019.00086.
- Laj, C., Channell, J., 2015. Geomagnetic excursions. In: Treatise on Geophysics. Elsevier, pp. 343–383. URL: https://linkinghub.elsevier.com/retrieve/pii/B9780444538 024001044 https://doi.org/10.1016/B978-0-444-53802-4.00104-4.
- Livermore, P.W., Hollerbach, R., Finlay, C.C., 2017. An accelerating high-latitude jet in Earth's core. Nat. Geosci. 10, 62–68. https://doi.org/10.1038/ngeo2859.
- Lund, S.P., Stoner, J., Channell, J., Lamy, F., 2006a. Detailed Paleomagnetic and Rock Magnetic Variability Within Three High-Resolution Study Intervals from Site 1233.
- Lund, S.P., Stoner, J., Lamy, F., 2006b. 2. Late Quaternary Paleomagnetic Secular Variation and Chronostratigraphy from ODP sites 1233 and 1234.
- Nakagawa, T., Davies, C.J., 2022. Combined dynamical and morphological characterisation of geodynamo simulations. Earth Planet. Sci. Lett. 594, 117752. URL: https://linkinghub.elsevier.com/retrieve/pii/S0012821X22003880 https://doi.org/10.1016/j.epsl.2022.117752.
- Nilsson, A., Holme, R., Korte, M., Suttie, N., Hill, M., 2014. Reconstructing holocene geomagnetic field variation: new methods, models and implications. Geophys. J. Int. 198, 229–248. https://doi.org/10.1093/gji/ggu120.
- Nilsson, A., Suttie, N., Korte, M., Holme, R., Hill, M., 2020. Persistent westward drift of the geomagnetic field at the core–mantle boundary linked to recurrent high-latitude weak/reverse flux patches. Geophys. J. Int. 222, 1423–1432. https://doi.org/ 10.1093/gi/ggaa249.
- Pais, M.A., Jault, D., 2008. Quasi-geostrophic flows responsible for the secular variation of the Earth's magnetic field. Geophys. J. Int. 173, 421–443. URL: https://academic.oup.com/gji/article-lookup/doi/10.1111/j.1365-246X.2008.03741.x https://doi.org/10.1111/j.1365-246X.2008.03741.x
- Panovska, S., Constable, C.G., Korte, M., 2018. Extending global continuous geomagnetic field reconstructions on timescales beyond human civilization. Geochem. Geophys. Geosyst. 19, 4757–4772. https://doi.org/10.1029/2018GC007966.
- Panovska, S., Korte, M., Constable, C.G., 2019. One hundred thousand years of geomagnetic field evolution. Rev. Geophys. 57, 1289–1337. URL: https:// onlinelibrary.wiley.com/doi/10.1029/2019RG000656. https://doi.org/10.1029/ 2019RG000656.
- Panovska, S., Korte, M., Liu, J., Nowaczyk, N., 2021. Global evolution and dynamics of the geomagnetic field in the 15–70 kyr period based on selected Paleomagnetic sediment records. J. Geophys. Res. Solid Earth 126. https://doi.org/10.1029/ 2021JB022681.